RESEARCH ARTICLE | NOVEMBER 26 2025

Band-filling and relaxation effects in the transient dielectric function of Ge

C. A. Armenta ⓘ ; M. Zahradník ⓘ ; M. Rebarz ⓘ ; C. Emminger ⓘ ; S. Espinoza ⓘ ; S. Vazquez-Miranda ⓘ ;
J. Andreasson ⓘ ; S. Zollner ✉ ⓘ

Check for updates

⤓ CHORUS

View Online   Export Citation

Articles You May Be Interested In

Excitonic effects at the temperature-dependent E_1 and $E_1 + \Delta_1$ critical points of Ge

J. Appl. Phys. (June 2025)

Transient dielectric function and carrier related processes in doped cubic GaN determined by femtosecond pump–probe spectroscopic ellipsometry

J. Appl. Phys. (September 2025)

Time-resolved pump–probe spectroscopic ellipsometry of cubic GaN II: Absorption edge shift with gain and temperature effects

J. Appl. Phys. (August 2023)

Band-filling and relaxation effects in the transient dielectric function of Ge

View Online   Export Citation   CrossMark

C. A. Armenta,[1] ID M. Zahradník,[2] ID M. Rebarz,[2] ID C. Emminger,[1] ID S. Espinoza,[2] ID S. Vazquez-Miranda,[2] ID
J. Andreasson,[2] ID and S. Zollner[1,a)] ID

AFFILIATIONS

[1]Department of Physics, New Mexico State University, MSC 3D, P. O. Box 30001, Las Cruces, New Mexico 88003-8001, USA
[2]ELI Beamlines Facility, The Extreme Light Infrastructure ERIC, Za Radnicí 835, 25241 Dolní Břežany, Czech Republic

Note: This paper is part of the Special Topic on Advances in Spectroscopic Ellipsometry Methods and Materials Characterization.
[a)]**Author to whom correspondence should be addressed:** zollner@nmsu.edu

ABSTRACT

This study investigates the transient dielectric function of germanium at charge carrier densities of the order of 10^{20} cm^{-3} using time-resolved spectroscopic ellipsometry. By employing a pump-probe technique, we explore the temporal evolution of the critical points E_1 and $E_1 + \Delta_1$ after high-intensity laser excitation. Given the two-dimensional character of these critical points, the absorption of Ge is significantly enhanced by excitonic binding. Furthermore, at high carrier densities, intervalley scattering and band saturation play a significant role in the optical response of the material. To address these phenomena, we combined band-filling effects with a two-dimensional excitonic line shape to model the observed optical spectra. We also simulated the Fermi energies and electron temperatures governing the measurements using Fermi–Dirac statistics. Given the short timescales of the carrier relaxation and intervalley scattering, this analysis focuses exclusively on the first few picoseconds after excitation, with a minimum step size of 50 fs. The model successfully reproduces the main features of the experimental spectra, capturing the reduction in amplitude of the dielectric function and the redshift of the critical points due to bandgap renormalization. From these fits, we extract an energy relaxation rate of the order of 1.5 meV fs^{-1} and provide a quantitative description of the ultrafast carrier dynamics in Ge.

I. INTRODUCTION

When a semiconductor is excited with a sufficiently energetic laser, electrons are promoted from the valence (VB) to conduction band (CB), which leads to a photoinduced increase in the density of charge carriers. These excited carriers will have excess energy that depends on the photon energy of the laser and electronic properties of the material. The excess energy can drive the carriers to highly excited states and take them out of thermal equilibrium with the lattice. After the initial excitation, these out-of-equilibrium carriers undergo diverse scattering and relaxation processes that affect the optical properties of the material. Moreover, processes, such as the initial thermalization, intervalley scattering, and cooling of the carriers, happen very quickly (of the order of 10^{-13} to 10^{-12} s).[1] The study of these ultrafast carrier dynamics, therefore, requires experimental techniques that are not only capable of probing the

material at different carrier densities, but also with sufficient temporal resolution to follow these processes.[1,2] Femtosecond pump-probe spectroscopic ellipsometry is ideal for analyzing these phenomena because it allows the distribution of carriers to vary as a function of the delay times.[3–7] Our analysis focuses on modeling the transient dielectric function (TDF) of Ge and describing its behavior as temperature and distribution of the carriers evolve. Specifically, we address the intervalley scattering of the carriers and band-filling effects within the first few picoseconds.

A. Ultrafast processes

In the absence of external fields or strong optical excitations, the subsystem of particles and quasi-particles within the lattice structure of a semiconductor remains in thermal equilibrium. In broad categorization, the distribution function of carriers and

phonons in this equilibrium state can be described by Fermi–Dirac and Bose–Einstein statistics, respectively. Under certain circumstances, the behavior of both subsystems can also be approximated with Maxwell–Boltzmann statistics. If, however, the equilibrium state is disrupted, the carriers will go out of thermal equilibrium with the lattice, and their combined average momentum will be non-zero. Furthermore, the carrier temperature may not only differ from that of the lattice, but also vary among carrier subspecies (electrons, holes, and excitons). In the case of optical excitation, if the energy of the light source used is larger than the bandgap of the semiconductor, some electrons are promoted from the VB to the CB, thereby leaving positively charged holes in their place. Once these carriers populate the excited states in the bands, they will undergo several relaxation processes that dissipate their corresponding excess energy and momentum.

These processes occur on very short timescales that can be divided into four different overlapping regimes.[1,2] In the coherent regime, which lasts only a few tens of femtoseconds, neither energy nor momentum has had any time to relax. Carriers have a strong coupling with the polarization of the electric field of the incident excitation radiation. Because of this coupling, the occupied states by the carriers are localized in energy and have a preferred direction in momentum space. This phase is followed by the non-thermal regime, where coherence is broken, and the distribution of the carriers is likely non-thermal (it cannot be described by a distribution function with a well defined temperature). Through different inelastic scattering processes, the carriers will establish a hot thermalized distribution, giving rise to the hot-carrier regime. At this stage, the carrier momentum initially induced by the polarization coupling with the incident radiation will have dissipated. Hence, there will be no preferred direction in momentum space. However, since the excess energy of the carriers is yet to be dissipated, the occupied states are still localized in energy. The momentum-relaxed carriers can now be described by a distribution function. Still, the temperature of this distribution function is usually greater than that of the lattice and might be different for each subspecies of carriers. Ultimately, the system enters the isothermal regime, where both energy and momentum begin to dissipate through elastic as well as inelastic scattering processes. The carriers are now in thermal equilibrium with the lattice. Diffusion and recombination of carriers take place, either radiatively or non-radiatively.

Although different scattering processes are the means of energy and momentum relaxation, it is only through scattering with the lattice that the carriers can relax in energy. Any other scattering process only redistributes energy among the different subspecies of carriers.[8] The initial excess energy of the carriers is given by[1]

$$E_e = \frac{\hbar\omega_{\text{pump}} - E_0}{1 - m_e/m_h},$$ (1a)

$$E_h = \hbar\omega_{\text{pump}} - E_0 - E_e,$$ (1b)

where E_0 is the bandgap energy, $\hbar\omega_{\text{pump}}$ is the energy of the optical excitation source, m is the effective mass, and the subscripts e and h stand for electrons and holes, respectively. By absorbing this excess energy, the carriers populate higher-energy states within the bands. As a consequence, the material's optical properties are modified in several ways.

B. Many-body effects

The presence of photo-excited carriers in the CB and VB modifies the energies of interband transitions. Exchange-correlation effects renormalize the bands and lower the transition energy of the bandgap and other critical points (CPs). On the other hand, due to phase-space filling, the chemical potential μ of the bands varies with the charge carrier density n. An increase in photo-excited electrons raises the quasi-Fermi energy $E_F^{(C)}$ above the CB minimum, while an increase in the hole population lowers the quasi-Fermi energy $E_F^{(V)}$ below the VB maximum. These competing effects are described by[1,9]

$$\overline{E}_g = \mu - E_F = E_{\text{xc}} + n\frac{\text{d}E_{\text{xc}}}{\text{d}n} - E_F,$$ (2)

where the over-line $\overline{E}_g$ indicates the renormalized energy gap and E_F is the total quasi-Fermi energy shift across the bands $[E_F = E_F^{(C)} + E_F^{(V)}]$. The chemical potential μ depends on the charge carrier density n and the exchange-correlation energy E_{xc}, which is given by Vashishta and Kalia as[10]

$$E_{\text{xc}} = \frac{a + br_s}{c + dr_s + r_s^2}R^{(x)}.$$ (3)

In Eq. (3), $R^{(x)}$ is the excitonic binding energy, the dimensionless quantity r_s is the average distance between carriers measured in units of the exciton Bohr radius, and the coefficients have the values $a = -4.8316$, $b = -5.0879$, $c = 0.0152$, and $d = 3.0426$. Renormalization lowers the energy of the gap and redshifts interband transitions. Conversely, the filling of the bands with photo-excited carriers has the opposite effect and raises the energies of these transitions. Since transitions at the absorption edge are blocked by the Pauli exclusion principle, bandgap or CP transitions need to occur higher up in the band. This is commonly known as the Moss–Burstein shift.[11,12] Moreover, at sufficiently high carrier densities, the absorption of the material decreases due to the saturation of available states for interband transitions.[13] In effect, the presence of photo-excited carriers within the bands will not only affect the energy of the transitions, but also reduce the absorption of the material. While raising both quasi-Fermi levels into their respective bands generally corresponds to population inversion, stimulated emission in Ge is not expected to play a significant role in the present work. Because Ge is an indirect gap semiconductor, any optical gain would occur near the direct bandgap (around 0.7 eV),[14] which is well below our probed spectral range. Although at lower densities than the ones presented here, previous studies of highly excited Ge have shown that no stimulated emission is observed.[13,15] Thus, the possibility of stimulated emission might reduce the carrier lifetimes, but does not affect the interpretation of our spectra at the E_1 and $E_1 + \Delta_1$ transitions.

26 November 2025 16:22:58

C. Diffusion of carriers

Another factor affecting the optical response of the material is the diffusion of carriers. In the case of optical excitation, excess carriers are generated only within the volume irradiated by the optical source. Once created, the carriers diffuse outside of this photoexcited volume. Therefore, the carrier density depends on both the penetration depth of the light source and the time after excitation. To get the initial concentration of carriers n_0 at time $t = 0$, Richter et al.[4] give a simple expression for the upper charge carrier concentration limit based on simple assumptions valid for low or moderate laser power,

$$n_0 \approx \frac{E_{\text{pulse}}}{\hbar\omega_{\text{pump}}}[1 - R(\theta, \omega)]\frac{4}{\delta\pi d_{\text{spot}}^2}. \quad (4)$$

Here, R is the reflectance at a given angle of incidence θ and frequency ω calculated from the complex dielectric function, δ is the penetration depth of the material, E_{pulse} is the energy of the pump pulse, and $\hbar\omega_{\text{pump}}$ is the photon energy of the pump. This simplified expression is only valid when the sample is a bare substrate. It is important to remark that the free carriers are excited at the surface of the sample rather than uniformly throughout the material. As a result, the carrier concentration exhibits a depth-dependent profile. Baron et al.[16,17] expressed this concentration as a function of both of these factors $n(x, t)$. Their study gives the profile of the carrier concentration at the surface where $x = 0$ as

$$n(t) = \frac{n_0}{4}\left[\text{erf}\left(\frac{t - \gamma_0}{\tau_0}\right) + 1\right]e^{\alpha^2 Dt - \frac{1}{\tau_1}}\text{erfc}\left(\sqrt{\alpha^2 Dt}\right), \quad (5)$$

where α is the absorption coefficient; $D \approx 67 \, \text{cm}^2/\text{s}$ is the ambipolar diffusion coefficient; τ_0 and τ_1 are the relaxation time and characteristic recombination time, respectively; and γ_0 is the position of the inflection point of the error function.

The initial carrier density, although it decreases with time, remains approximately constant during the first few picoseconds.[6] The onset of vertical carrier diffusion can be estimated from the diffusion time[14] $t_D = \delta^2/D \approx 7 \, \text{ps}$. This diffusion time is a lower limit since the penetration depth of the laser might be larger for high laser power due to bleaching of the absorption. We conclude that vertical carrier diffusion will play only a moderate role within the first few picoseconds after laser excitation. Lateral diffusion of carriers is much slower, because the spot size is much larger than the penetration depth.

Furthermore, if the penetration depth of our sample at the pump wavelength (the photoexcitation light source) is significantly greater than at the probing wavelength, the carrier density as a function of depth can be approximated as constant. Therefore, in the present work, given the timescale and the photon energy range at which we are probing, we will only use Eq. (4) to estimate the carrier density and keep it constant throughout time. These assumptions are further validated by previous studies on carrier diffusion in highly excited bulk Ge.[18,19]

II. EXPERIMENTAL SETUP

Figure 1(a) shows the femtosecond ellipsometry configuration. The Coherent Astrella (35 fs, max. 6 mJ) laser emits pulses of 800 nm wavelength at a 1 kHz repetition rate.[20] This beam is then divided into the pump and probe pulses. The pump pulse is directed to a 250 Hz chopper before propagating through the delay line (DL). The temporal resolution of the DL is about 3 fs and capable of up to a 6.67 ns pump-probe delay. After the DL, the beam is directed toward a focusing lens, which adjusts the pump

(a)

(b)
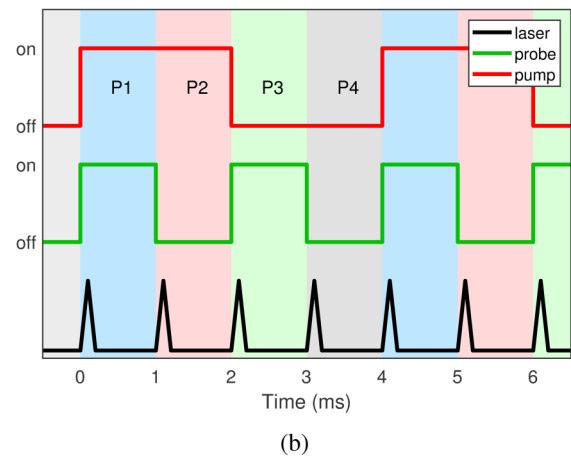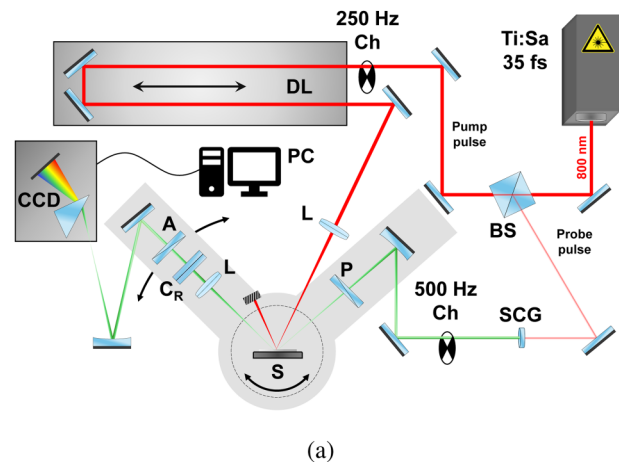
FIG. 1. (a) Schematic of the broadband femtosecond spectroscopic ellipsometry setup. A beam splitter **BS** splits the initial infrared pulse into the pump and probe pulse. In the pump path, the pulse goes through a 250 Hz chopper **Ch**, the delay line **DL**, a focusing lens **L**, and the sample **S**. In the probe path, the pulse is redirected to a CaF$_2$ plate that transforms the infrared pulse into white light via supercontinuum generation (**SCG**). This white light probe pulse then goes trough a rotating compensator ellipsometry stage [polarizer (**P**), sample (**S**), rotating compensator (**C$_R$**), and analyzer (**A**)], before hitting the **CCD** detector. (b) The two choppers of the experimental setup give rise to four different intensity channels. P1, *pump + probe*; P2, *pump only*; P3, *probe only*; and P4, *dark*.

26 November 2025 16:22:58

beam-spot diameter before it reaches the sample stage. By adjusting this diameter, we are able to modulate the number of photons per unit area. For the measurements presented in this work, the beam diameter and pump power recorded were $305\,\mu$m and 3.0 mW, respectively. The probe pulse, on the other hand, is focused by a lens onto a CaF_2 plate, which generates white light from the initial IR pulse by means of supercontinuum generation (SCG). This probe pulse has a spectral range of 1.3–3.6 eV and accounts for only about $1\,\mu$J of the original laser pulse energy. After passing through a 500 Hz chopper, the probe then goes through a conventional rotating compensator ellipsometry setup. Polarizer and analyzer are set $90°$ from each other. The compensator will rotate for a number of angles between 30 and 40. Finally, the reflected probe pulse is dispersed by a prism before arriving to the CCD detector.

As is the case in typical pump-probe spectroscopy setups, the measured signal is not the same as in the steady-state case (in our case, the ellipsometric angles Ψ and Δ), but rather comprises the reflectance-difference spectra $\Delta R(E, \Delta t)$. They are not only a function of wavelength (or photon energy E), but of time delay Δt as well. As depicted in Fig. 1(b), the choppers in our setup create four channels: *Pump + probe*, *pump only*, *probe only*, and *dark* (labeled P1, P2, P3, and P4 in Fig. 1). The four measured intensities are related to the reflectance-difference by

$$\frac{\Delta R(E, \Delta t)}{R^0(E)} = \frac{R^{\mathrm{p}}(E, \Delta t)}{R^0(E)} - 1 \equiv \frac{I_{\mathrm{P}_1} - I_{\mathrm{P}_2}}{I_{\mathrm{P}_3} - I_{\mathrm{P}_4}} - 1. \tag{6}$$

In Eq. (6), $R^{\mathrm{p}}(E, \Delta t)$ are the background-corrected *pump + probe* spectra, $R^0(E)$ is the *probe only* spectrum, and I_{P_j} is the intensity of the jth channel. We use the reflectance-difference to obtain the intensity (at a given compensator angle) with the expression

$$I(E, \Delta t) = I^0(E)\left[1 + \left(\frac{\Delta R(E, \Delta t)}{R^0(E)}\right)\right], \tag{7}$$

where $I^0(E)$ is the pseudo-intensity spectra computed using $\Psi^0(E)$ and $\Delta^0(E)$ from a steady-state ellipsometry reference measurement of the sample of interest. Using this intensity, we can obtain the Mueller matrix of the sample by the Moore–Penrose pseudo-inversion formalism.[3] The final Mueller matrix for an isotropic sample is given as[21]

$$M_{\mathrm{S}} = \begin{bmatrix} 1 & -N & 0 & 0 \\ -N & 1 & 0 & 0 \\ 0 & 0 & C & S \\ 0 & 0 & -S & C, \end{bmatrix} \tag{8}$$

where $N = \cos 2\Psi$, $C = \sin 2\Psi \cos \Delta$, and $S = \sin 2\Psi \sin \Delta$. We can use the values of matrix (8) to obtain the ellipsometric angles in terms of the sample Mueller matrix components in the following form:[21]

$$\Psi = \frac{1}{2}\arctan\left(\frac{\sqrt{C^2 + S^2}}{N}\right), \tag{9a}$$

$$\Delta = \frac{1}{2}\arctan\left(\frac{S}{C}\right). \tag{9b}$$

Once the ellipsometric angles are known, we can use the expression[21]

$$\langle \varepsilon \rangle = \sin^2 \theta \left[1 + \tan^2 \theta \left(\frac{1 - \rho}{1 + \rho}\right)^2\right] \tag{10}$$

to obtain the pseudo-DF $\langle \varepsilon \rangle$ as a function of delay time and energy. In Eq. (10), θ is the angle of incidence and ρ is the complex reflectance ratio calculated with the ellipsometric angles as[21]

$$\rho = \tan \Psi e^{i\Delta}. \tag{11}$$

Because we are interested only in the bulk material, it is necessary to correct for the oxide overlayer that is present at the moment of the measurement. To make this oxide correction, we use the optical properties of GeO_2 published by Nunley *et al.*[22] and a parametric semiconductor oscillator model for Ge by Emminger *et al.*[23] The procedure consists of first fitting the measured pseudo-dielectric function to determine the surface overlayer thickness. In the second step, we fix the overlayer thickness to its value determined in the first step and determine the substrate optical constants at each delay time from a point-by-point fit.[21] We achieved this with the aid of the commercial software WVASE32, from the J. A. Woollam company.[24]

A sample of bulk Ge was measured at an AOI of $65°$ and with a p-polarization state for the pump. Delay times ranged from -5 ps to 1 ns with varying step sizes. The smallest step size was 50 fs (from -0.5 to 1.5 ps). A total of 34 compensator angles were measured for each time delay. Figure 2 shows the real and imaginary part of ϵ over an energy range of 1.8–3 eV after the oxide correction. To overcome statistical fluctuations, about 400 reflectance-difference spectra per data point (after clearing outliers) are averaged. For more details on the data acquisition process, see Sec. S1 in the supplementary material. If interested in more information about the experimental setup, we encourage the reader to look at Ref. 3.

III. THEORY

The decoherence and thermalization timescales of Ge vary within the literature.[6,25–27] Nonetheless, the upper limit for the thermalization time of the initial population of photo-excited carriers is agreed upon to be a hundred femtoseconds.[6,14,26,28] Decoherence happens at even shorter timescales, not surpassing a few tens of femtoseconds.[1,2,27] Due to the fast intervalley scattering rate ($\lesssim 50$ fs), the energy of the carriers can be dissipated even if they are still not in the thermal regime. Lastly, excited carriers tend to have a very long lifetime in Ge, lasting up to nanoseconds.[1] At our high carrier concentrations, the dominant recombination mechanism is Auger recombination, which has a rate of $\tau^{-1} = \alpha n_0^2$ where $\alpha = 2 \times 10^{-30}$ cm^6 s^{-1} is the Auger coefficient.[14] For $n_0 = 10^{20}$ cm^{-3}, $\tau = 50$ ps, which is much slower than the relevant timescale of our experiment. For polished Ge, surface recombination can be ignored.[6] Radiative and Schottky–Reed–Hall (defect) recombination are much slower. Once thermalized, the carriers can be described by a distribution function, which, given the carrier
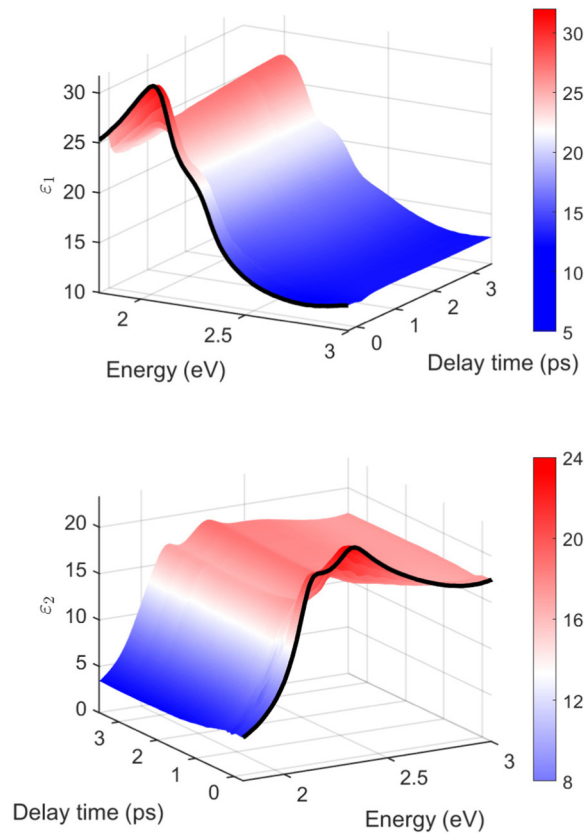
FIG. 2. Real (top) and imaginary (bottom) part of the point-by-point dielectric function fit as a function of photon energy (from 1.8 to 3 eV) and delay time (from -0.25 to 3.5 ps).

densities generated in our experiment, is degenerate. Consequently, we simulated the ultrafast dynamics of the carriers using Fermi–Dirac statistics, which in turn enabled us to model the measured TDF. Figure 3(a) provides a qualitative overview of the initial dynamics induced by the high-intensity laser pulse during the measurements.

A. Initial excitation

At 1.55 eV, the infrared pump laser is energetic enough to promote electrons from the heavy-hole (hh), light-hole (lh), and split-off (SO) VBs to the CB. This excitation of carriers occurs near the Γ-point of the Brillouin zone. For a non-degenerate distribution, the excess energy E_e of the carriers in the CB of Eq. (1) has previously been correlated with the effective carrier temperature T_c as[9]

$$E_c = 3k_B T_c, \quad (12)$$

where k_B is the Boltzmann constant. Since this expression is valid for both electrons and holes, we used the subscript c (which labels the carriers $\equiv e, h$). However, at high carrier densities, where the

distribution is degenerate, obtaining the effective carrier temperature becomes a more involved process. Nevertheless, by equating the energy of the total number of absorbed photons to the total energy of the electron–hole distribution, Smirl obtained a similar effective carrier temperature expression for a Fermi-like distribution.[27] Therefore, for the present work, we used Eq. (12) to estimate an initial effective carrier temperature of 2500 K. As the initial hot electrons cool down, they rapidly scatter to the satellite valleys (L- and X-valleys), eventually accumulating in the L-valley due to its lower energy.[5,6] Intervalley scattering in Ge has been studied extensively over the years, and the rates of scattering have (for the most part) an agreed upon value.[19,25,26,29–32] However, we will not concern ourselves with these scattering rates. Instead, our approach will be to calculate the density of carriers that each valley allows as a function of temperature. The carrier population at each valley will depend on their corresponding density of states. Once we know how the carrier distribution behaves for each temperature of the carriers, we can calculate the optical response as a function of this carrier temperature and then compare it with the experimental data.

B. Carrier statistics

As shown in Fig. 3(b), the change in the electron population of the CB (and the hole population of the VB) yields a quasi-Fermi energy $E_F^{(C)}$ above the CB minimum [and $E_F^{(V)}$ below the VB maximum]. After intervalley scattering takes place, the excited electrons will populate the different valleys of the CB. When electrons occupy the previously empty CB states, the band becomes partially filled, which reduces interband transition strengths into those states. As a result, the material's absorption is diminished. Therefore, to account for band-filling effects, we must first estimate the initial carrier density, which determines the shift in the quasi-Fermi energy.

Previous studies have shown that, due to its higher density of states, electrons initially scatter to the X-valley before settling at the L-valley.[6] Within a few picoseconds, however, almost the entire X-valley electron population scatters out of this valley and relocates to the L-valley.[32] This is shown by the dotted magenta arrows in Fig. 3(b). As a side note, in the present work, we will ignore the change in the quasi-Fermi energy in the VB. This is because, while we are interested in the chemical potential of Eq. (2), the photo-generated holes are confined to the Γ-valley and do not influence the VB at other points in the band structure. The zone at which we are probing, on the other hand, is near the L-valley (where E_1 and $E_1 + \Delta_1$ CPs are located). Therefore, the change in $E_F^{(V)}$ does not affect the interband transitions in the probing region.

Although intervalley scattering redistributes the carriers among the entire CB, the initial carrier density is determined solely by direct bandgap transitions (since photo-excited carriers are primarily generated at the Γ-valley, we are ignoring indirect bandgap transitions).[33] By measuring the power and beam-spot diameter of the pump, we can use Eq. (4) to estimate the initial carrier density in the limit of low or moderate laser power (where no bleaching of the absorption due to band filling occurs, i.e., $\mu \ll E_0 + E_e$). In this limit and with Eq. (12) for the initial carrier temperature, we can use the expression[34]
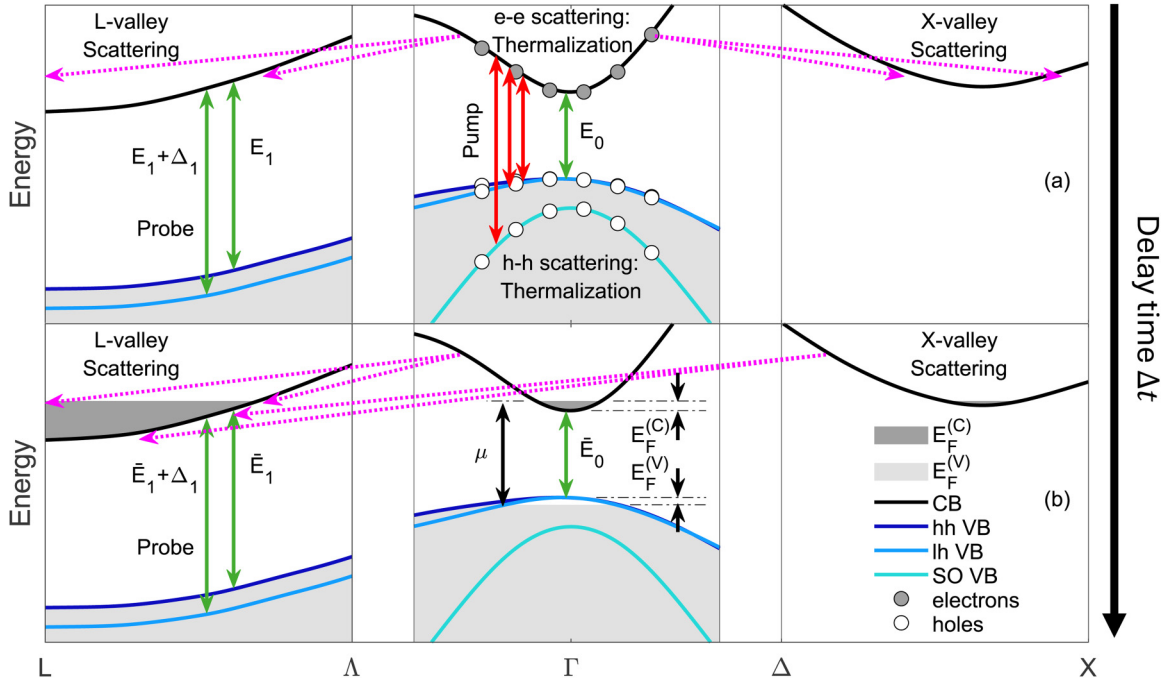
FIG. 3. (a) Band diagram at the initial moment of excitation. The pump pulse (red arrows) promotes electrons (gray circles) from the heavy-hole (blue), light-hole (light blue), and split-off (cyan) valence bands to the conduction band (black) near the Γ-point. The pump pulse also creates holes (white circles) in the valence bands. Once in the conduction band, the electrons thermalize and scatter to the L- and X-valleys. (b) Diagram after some delay time Δt. The thermalized electrons and holes adjust the quasi-Fermi energy of the bands [$E_F^{(C)}$ for the conduction band (dark gray area) and $E_F^{(V)}$ for the valence band (light gray area)]. Electrons in the conduction band eventually relocate from the X-valley to the L-valley (the lowest conduction band valley). At this stage, the energy required to move the electrons from the valence band to the conduction band is given by the quasi-Fermi energies $E_F^{(C)}$ and $E_F^{(V)}$ plus the renormalized bandgap [this is the definition of the chemical potential μ (black arrow)].

$$n_\Gamma(T,\mu) = \frac{1}{4}\left(\frac{2m_\Gamma k_B T}{\pi\hbar^2}\right)^{3/2} F_{1/2}\left(\frac{\mu - E_0}{k_B T}\right) \quad (13)$$

to solve for the chemical potential μ at a given temperature T and carrier density n_Γ of carriers in the Γ-valley (for parabolic bands suitable in the low-power limit). The terms $\hbar$, $F_{1/2}$, m_Γ, and E_0 in Eq. (13) are the reduced Planck constant, the complete Fermi integral of order $1/2$, and the effective electron mass in the Γ-valley, respectively. Although Eq. (13) is not analytically invertible, we can use Eq. (12) to calculate the effective carrier temperature and transform the dependence of the carrier density from $n_\Gamma(\mu, T) \rightarrow n_\Gamma(\mu)$. We then solve numerically for μ. To compute the complete Fermi integral, we note that $F_j(x) = -\text{Li}_{j+1}(-e^x)$, where Li is the polylogarithm function. This allows us to use the MATLAB polylogarithm function polylog(n,x).[35] Unfortunately, this procedure yielded a chemical potential that exceeded the energy of the pump pulse, which is an unphysical result that violates our assumption of low or moderate laser power stated above.

Therefore, we evaluate the carrier concentration in the limit of high laser power and set the chemical potential in Eq. (13) equal to the excess energy E_e induced by the pump given by Eq. (1). We also incorporate non-parabolicity effects by using the expressions for the carrier densities at each valley given by Menéndez et al.,[36]

$$n_\Gamma(T,\mu) = \frac{1}{4}\left(\frac{2m_\Gamma k_B T}{\pi\hbar^2}\right)^{3/2}\left[F_{1/2}\left(\frac{\mu - E_0}{k_B T}\right) + \frac{15}{8}\left(\frac{k_B T}{\Delta_\Gamma}\right)F_{3/2}\left(\frac{\mu - E_0}{k_B T}\right)\right], \quad (14a)$$

$$n_L(T,\mu) = \left(\frac{2m_L k_B T}{\pi\hbar^2}\right)^{3/2}\left[F_{1/2}\left(\frac{\mu - E_{\text{ind}}}{k_B T}\right) + \left(\frac{k_B T}{\Delta_L}\right)F_{3/2}\left(\frac{\mu - E_{\text{ind}}}{k_B T}\right)\right], \quad (14b)$$

$$n_X(T,\mu) = \frac{3}{2}\left(\frac{2m_X k_B T}{\pi\hbar^2}\right)^{3/2}\left[F_{1/2}\left(\frac{\mu - E_X}{k_B T}\right)\right], \quad (14c)$$

where the terms $\Delta_\Gamma = (3/2)[2/E_0 + 1/(E_0 + \Delta_0)]^{-1}$ and $\Delta_L = [1/E_1 + 1/(E_1 + \Delta_1)]^{-1}$ are the characteristic non-parabolicity energies. The terms m_Γ, m_L, m_X, E_0, E_{ind}, and E_X correspond to the masses and CB minima of the Γ-, L-, and X-valleys, respectively. It should be mentioned that Eqs. (13) and (14a) are valid only at $\Delta t = 0$ (for very short times, before intervalley scattering becomes important after 20–50 fs). The small effective mass in the Γ-valley pushes the quasi-Fermi level high above the CB minimum. Important parameters, such as bandgaps and effective masses, are given in Table I.

TABLE I. Conduction band energy minima and effective masses in free electron mass m_0 units for the different valleys of the band structure of Ge at room temperature.

E_0 (eV)	Δ_0 (eV)	E_{ind} (eV)	Δ_1 (eV)	E_X (eV)	m_Γ	$m_{\perp,L}$	$m_{\parallel,L}$	$m_{\perp,X}$	$m_{\parallel,X}$
0.805[a]	0.287[b]	0.660[c]	0.200[d]	0.84[e]	0.042[f]	0.083[g]	1.58[g]	0.20[e]	0.80[e]

[a]Reference 37.
[b]Reference 38.
[c]Reference 36.
[d]Reference 39.
[e]Reference 40.
[f]Reference 41.
[g]Reference 42.

With the chemical potential limited by the excess energy of the pump, the Fermi integrals in Eqs. (14) become $F_j(E_e/k_B T_e)$. Figure 4 shows the carrier density at the Γ-valley of Eq. (14a) as a function of the effective carrier temperature. Again, this temperature is calculated using Eq. (12). Because electrons quickly scatter to the L- or X-valley (at a rate of up to $10^{14}\,\mathrm{s^{-1}}$),[33] we do not expect saturation of carriers at the Γ-valley.[30] Therefore, to account for the additional carriers enabled by intervalley scattering, we also plot $2 \times n_\Gamma(T)$, twice the density of Eq. (14a). The result is a density range between 5×10^{19} and $10^{20}\,\mathrm{cm^{-3}}$ at an effective carrier temperature of about 2500 K.

With this carrier density estimate, we include intervalley scattering by summing the carrier densities across all valleys,

$$n_e(T,\mu) = n_L(T,\mu) + n_\Gamma(T,\mu) + n_X(T,\mu), \quad (15)$$

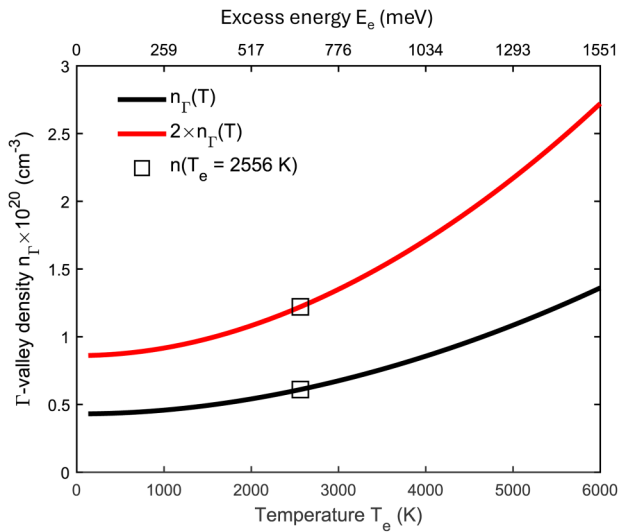where $n_L(T,\mu)$, $n_\Gamma(T,\mu)$, and $n_X(T,\mu)$ are given by Eq. (14). Since we know the effective temperature of the carriers, we can solve for μ in Eq. (15) as a function of temperature in the same manner as before. It is important to remark that, independent of the relative density of carriers at each valley, the chemical potential is the same for all valleys. We make this assumption for times greater than 100 fs based on the discussions of Refs. 30 and 43. Figure 5(a) shows the chemical potential as a function of the carrier temperature for the estimated densities (5×10^{19} and $10^{20}\,\mathrm{cm^{-3}}$). At low temperatures, the chemical potential lies above the indirect bandgap, as expected and shown in Fig. 3(b). At higher temperatures, however, the chemical potential drops below the bandgap. The cooling of the initial hot carriers in our experiment should lead to an increase in the chemical potential, as indicated by the curves shown in Fig. 5(a). Figure 5(b) shows the percentage of carriers at each valley as a function of temperature for the aforementioned carrier densities. At high

FIG. 4. Charge carrier density of the Γ-valley as a function of the initial electron temperature T_e. The black line is given by Eq. (14a) (infinite intervalley scattering time), and the red line is the same density multiplied by 2 (intervalley scattering time equals half the duration of the laser pulse). The squares (□) show the density at the effective carrier temperature given in Eq. (12) for our experimental condition.

FIG. 5. (a) Chemical potential as a function of electron temperature for a density of $5 \times 10^{19}\,\mathrm{cm^{-3}}$ (black line) and $10^{20}\,\mathrm{cm^{-3}}$ (red line), calculated from Eq. (15) in thermal equilibrium for times much larger than the intervalley scattering times. The squares (□) show the chemical potential at the effective carrier temperature given in Eq. (12). (b) The relative population density of the Γ-, L-, and X-valleys (black, blue, and red, respectively) calculated from Eqs. (14) with respect to the total density of Eq. (15).

26 November 2025 16:22:58

temperatures, the carriers are roughly equally distributed between the L- and X-valley. However, as the carriers cool down, they relax toward the L-valley. The density at the Γ-valley, on the other hand, remains close to zero at all temperatures. This confirms previous observations of the insignificant role that the central valley plays in allocating carriers.[30] Ultimately, any saturation of the absorption in the Γ-valley is a direct result of the buildup of the population of carriers in the satellite valleys.

C. Dielectric function

As seen in Fig. 3, the VBs run parallel to the CB in the Λ-direction. This creates the van Hove singularities E_1 and $E_1 + \Delta_1$.[44] These transitions occur from the hh and lh band to the CB, respectively. Once the carriers are photo-generated, the interaction between the electron–hole pairs tends to form excitons. Furthermore, because of the joint density of states (JDOS) of these transitions, the excitonic systems for E_1 and $E_1 + \Delta_1$ are confined to a two-dimensional plane. To describe the optical response for this system, Tanguy provided an expression for the complex DF that incorporates the effects of two-dimensional Wannier excitons.[45] More importantly for the present work, Tanguy's model has already been adapted to the aforementioned CPs of Ge.[46] For the CP E_1, the DF takes the form[46]

$$\varepsilon(E) = \frac{A}{\pi(E + i\Gamma)^2}\{g_a[\xi(E + i\Gamma)] + g_a[\xi(-E - i\Gamma)] - 2g_a[\xi(0)]\},$$

(16)

where

$$A = \frac{4e^2\mu_\perp \overline{P}^2}{3\pi\varepsilon_0 m_0^2}k_{\max}, \quad \xi(z) = \sqrt{\frac{R^{(x)}}{E_1 - z}},$$

$$\text{and} \quad g_a(\xi) = 2\ln(\xi) - 2\psi\left(\frac{1}{2} - \xi\right).$$

(17)

In Eq. (17), the amplitude A depends on the electron charge e, the free electron mass m_0, the permeability of free space ε_0, the reduced mass of the two-dimensional exciton $\mu_\perp$ (fitted as described in Sec. IV), the average momentum matrix element $\overline{P}$, and the maximum wave vector range $k_{\max}$ where transitions take place, whereas the argument ξ depends on the exciton's binding energy $R^{(x)}$, see Eq. (7) in Ref. 46, and the CP energy E_1. ψ is the complex digamma function. This model is only valid for steady-state measurements, which allows us to study non-equilibrium conditions. See Sec. IV A of Ref. 46 for a discussion of the values of $\overline{P}$ and $k_{\max}$.

Band-filling effects in the DF of Ge have previously been explored in the literature (see Sec. S2 for more details).[39,47] By incorporating a Fermi–Dirac probability distribution to the DF for uncorrelated electron–hole pairs, Xu et al. give the expression[47]

$$\varepsilon_2(E) = \frac{A}{2k_{\max}E^2}H(E - E_1)\int_{-k_{\max}}^{k_{\max}}dk_z\left\{1 - f\left[E_C\left(E, k_z^2\right)\right]\right\}, \quad (18)$$

where A is given in Eq. (17), and

$$E_C\left(E, k_z^2\right) = E_{\text{ind}} + \frac{\hbar^2 k_z^2}{2m_\parallel} + (E - E_1)\frac{\mu_\perp}{m_\perp}. \quad (19)$$

We can incorporate band-filling effects into the excitonic model by noting that the integral in Eq. (18) only modifies the amplitude of the DF. Therefore, we can replace the amplitude in the excitonic line shape with the one obtained from band-filling considerations. Our probing region contains the CPs E_1 and $E_1 + \Delta_1$. Therefore, we require two similar expressions to account for both CPs. The energy, broadening, reduced mass, and exciton binding energy need to be adjusted separately for each CP. Our final result is

$$\varepsilon_2(E) = A^{(E_1)}\text{Im}\left\{\frac{g_a\left[\xi^{(E_1)}(E + i\Gamma^{(E_1)})\right] + g_a\left[\xi^{(E_1)}(-E - i\Gamma^{(E_1)})\right] - 2g_a\left[\xi^{(E_1)}(0)\right]}{\left[E + i\Gamma^{(E_1)}\right]^2}\right\}\int_{-k_{\max}}^{k_{\max}}dk_z\left\{1 - f\left[E_C^{(E_1)}\left(E, k_z^2\right)\right]\right\}$$

$$+ A^{(E_1+\Delta_1)}\text{Im}\left\{\frac{g_a\left[\xi^{(E_1+\Delta_1)}(E + i\Gamma^{(E_1+\Delta_1)})\right] + g_a\left[\xi^{(E_1+\Delta_1)}(-E - i\Gamma^{(E_1+\Delta_1)})\right] - 2g_a\left[\xi^{(E_1+\Delta_1)}(0)\right]}{\left[E + i\Gamma^{(E_1+\Delta_1)}\right]^2}\right\}\int_{-k_{\max}}^{k_{\max}}dk_z\left\{1 - f\left[E_C^{(E_1+\Delta_1)}\left(E, k_z^2\right)\right]\right\},$$

(20)

where

$$A^{(E_1)} = \frac{2e^2\mu_\perp^{(E_1)}\overline{P}^2}{3\pi\varepsilon_0 m_0^2}, \quad \xi^{(E_1)}(z) = \sqrt{\frac{R^{(E_1)}}{E_1 - z}},$$

$$\text{and} \quad E_C^{(E_1)}\left(E, k_z^2\right) = E_{\text{ind}} + \frac{\hbar^2 k_z^2}{2m_\parallel} + (E - E_1)\frac{\mu_\perp^{(E_1)}}{m_\perp}$$

(21)

for E_1, and

$$A^{(E_1+\Delta_1)} = \frac{2e^2\mu_\perp^{(E_1+\Delta_1)}\overline{P}^2}{3\pi\varepsilon_0 m_0^2}, \quad \xi^{(E_1+\Delta_1)}(z) = \sqrt{\frac{R^{(E_1+\Delta_1)}}{E_1 + \Delta_1 - z}},$$

$$\text{and} \quad E_C^{(E_1+\Delta_1)}\left(E, k_z^2\right) = E_{\text{ind}} + \frac{\hbar^2 k_z^2}{2m_\parallel} + (E - E_1 - \Delta_1)\frac{\mu_\perp^{(E_1+\Delta_1)}}{m_\perp}$$

(22)

for $E_1 + \Delta_1$. The real part of Eq. (20) can be computed with a Kramers–Kronig transformation (typically, we also add a constant offset ε_{off} to the real part of the DF, to account for additional non-resonant contributions from other interband transitions).[46] The supplementary material shows a compact expression for the integrals over the z-axis in k-space using the Fermi integral $F_{-1/2}$.

IV. FITTING PROCEDURE

We now proceed to fit our model to the experimental data. The expression in Eq. (20) has six fitting parameters: carrier temperature T_c, carrier density n, and the energy and broadening of the CPs (E_1, $E_1 + \Delta_1$, $\Gamma^{(E_1)}$, and $\Gamma^{(E_1+\Delta_1)}$). At first glance, it might appear that the chemical potential μ is another free parameter. However, as stated in Eqs. (15) and (14), the value of μ depends on T_c and n. Moreover, based on our carrier density estimates in Sec. III B, the value of the carrier density must be restrained to be between 5×10^{19} and 10^{20} cm^{-3}. Consequently, the carrier density is held constant for all delay times. Conventionally, the energy and broadening of the CPs are extracted by fitting the 2nd derivative of the DF, rather than the DF itself. In contrast, the change in the chemical potential induced by variations in the carrier temperature and density affects primarily the DF, not its derivative. Furthermore, to capture the induced reduction in the amplitude of the DF, we need a near perfect match of the fitted model at the CP absorption peaks.

To overcome these challenges, we introduced the reduced masses $\mu_\perp^{(E_1, E_1+\Delta_1)}$ as additional fitting parameters as in Ref. 46 and divided the fitting process into two steps. Initially, we performed a 2nd derivative fitting of Eq. (20) for the negative time delays while holding the chemical potential equal to its theoretical value at room temperature (see Sec. S3 in the supplementary material for this calculation). This yielded the values for the energy and broadening of the CPs. Subsequently, we fitted $\mu_\perp^{(E_1, E_1+\Delta_1)}$ to the DF. If any discrepancies in their corresponding 2nd derivatives appeared between the model and experimental data, the two-step procedure was repeated until no further change was observed. In this manner, we ensured that the final values of the reduced masses were those required to achieve an accurate fit to both the DF and its 2nd derivative. The obtained values for the reduced masses were $\mu^{(E_1)} = 0.0566$ and $\mu^{(E_1+\Delta_1)} = 0.0558$. While the energies and broadenings of the critical points may vary with carrier temperature and density, we assume that the reduced masses will remain constant. This assumption is based on the lack of influence of carrier temperature on the reduced masses. In essence, reduced masses are only affected by the red-shift of thermal expansion.[46,48] Hence, they are not directly influenced by photoexcited carriers.

With this in mind, the positive delay time data were fitted using the reduced masses obtained from the previous fitting procedure. Again, to obtain the carrier temperature, we fitted the experimental DF, rather than its 2nd derivative. The carrier temperature and density were constrained to the previously calculated values of Sec. III B, but with a variation margin of $\pm 5\%$. Although this approach provides reasonable estimates for the carrier temperature (and by extension, the chemical potential), the resulting energy and broadening parameters of the CPs are less reliable. For these latter

parameters, a 2nd derivative analysis offers more accurate characterization. However, when compared with experimental data, the results obtained from this latter method were not as good as with the previous (see Figs. S10 and S11 in the supplementary material). This discrepancy is not unexpected, as the energy and broadening extracted from each method inherently differ depending on what is being fitted. In particular, fitting unmodulated data, such as the DF, yields different results than fitting its derivative, and even within derivative-based methods, the extracted parameters can depend on the order of the derivative used[49,50] and the energy interval fitted.

To compute the 2nd derivative of the data, we used an extended Gauss (EG) digital filter to suppress the noise and smooth the experimental data.[51] We then convoluted the DF with the derivative of the filter to obtain the desired derivative (see Sec. S4 for more information on this procedure). The EG filter is defined in direct space as[52,53]

$$ b_M(x) = \sum_{m=0}^{M} \left[(-1)^m \frac{\Delta E^m}{m!} \frac{d^m}{d\Delta E^m} \right] \frac{\exp[-x^2/(4\Delta E^2)]}{2\sqrt{\pi}\Delta E}, \quad (23) $$

where we selected $M = 4$ according to the discussion in Ref. 52. The filter width ΔE was determined by identifying the white noise onset in the Fourier coefficients of the data.[7] For consistency, the derivative of the model must be computed in the same manner as the derivative of the experimental data.[49] Therefore, we convoluted Eq. (20) with the same EG filter (and the same filter width ΔE) while leaving the fitting parameters free. In Sec. V, we present the results from directly fitting the DF. For the results of the 2nd derivative analysis and details on the EG filter, see Sec. S4 in the supplementary material.

V. RESULTS AND DISCUSSION

Figures 6(a) and 6(b) show the experimental data and corresponding fit results for the imaginary part of the TDF $\varepsilon_2(E, \Delta t)$ from -0.5 to 3 ps, respectively. The spectrum at negative delay times is shown in black. Spectra at positive delay times are color-coded according to the delay time: early delays are represented by red tones, while later delays progress toward blue along the color scale. Because negative delay times correspond to pre-excitation data (steady-state measurement shown in black), the chemical potential and temperature for the model are that of an intrinsic semiconductor at room temperature (see Sec. S3 in the supplementary material). With positive delays, however, the temperature of the carriers is high and the chemical potential changes accordingly. As delay time progresses, the cooling of the carriers increases the chemical potential according to the calculations from Sec. III B. As a result, the amplitude of $\varepsilon_2(E, \Delta t)$ decreases with each delay measurement. As can be seen in Fig. 6, the model captures the reduction in the amplitude of the spectra very well, especially near the CPs E_1 and $E_1 + \Delta_1$. At low and high energies, the contributions of other interband transitions are omitted; hence, the amplitude of the theoretical model is smaller than in the experimental data.
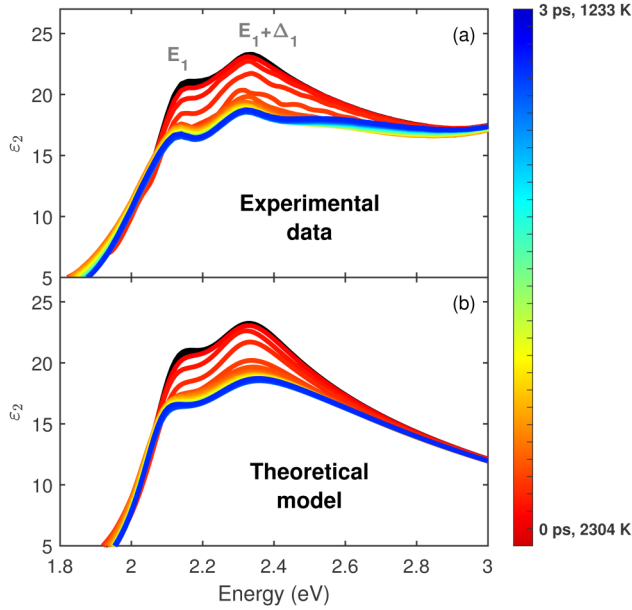
26 November 2025 16:22:58

FIG. 6. (a) Imaginary part of the transient dielectric function of Ge $\varepsilon_2(E, \Delta t)$. Negative delays are shown in black, whereas the color scale represents the delay times from -0.1 (red) to 3 ps (blue). (b) Theoretical model fitted to the data, where the color scale represents the carrier temperature (the red to blue color scale represents high to low temperatures).

A. Carrier relaxation

Along with the theoretical curve for a carrier density of $10^{20}\,\mathrm{cm}^{-3}$ of Fig. 5(a), Fig. 7 shows the fitted chemical potential plotted against the carrier temperature. As this fitted parameter (circles) follows the calculated curve for μ, the carriers relax and cool down. At 1 ps, the cooling of the carriers seems to slow down, indicating the relaxation in energy of the electrons to the bottom of the CB. By using the relation[9]

$$T_{\mathrm{c}}(t) = -\frac{C}{3k_{\mathrm{B}}} \int_0^t \left| \left\langle \frac{\mathrm{d}E}{\mathrm{d}t} \right\rangle \right| \mathrm{d}t + T_0, \tag{24}$$

we can estimate the energy relaxation rate as a function of delay time, as shown by the red line in Fig. 8. In Eq. (24), T_0 is the carrier temperature at infinite (or negative) time delays and C is a dimensionless factor that accounts for the reduction in the energy lost by screening of the electron–phonon interaction and non-equilibrium phonons (in general, C must be less than unity).[2,9] In our case, because of the short wavelengths associated with the phonon branches, $C \approx 1$. Note in Fig. 8 that the electron temperature never reaches room temperature, hence the obtained large value of T_0 in Eq. (24) ($\sim$1227 K). This is likely due to the exclusion of excitonic screening in our calculations. We will expand on this when we discuss limitations of the theory in Sec. V B. The functional form of $\langle \mathrm{d}E(t)/\mathrm{d}t \rangle$ depends on the diverse phonon scattering mechanics responsible for energy relaxation.[8,54] To simplify
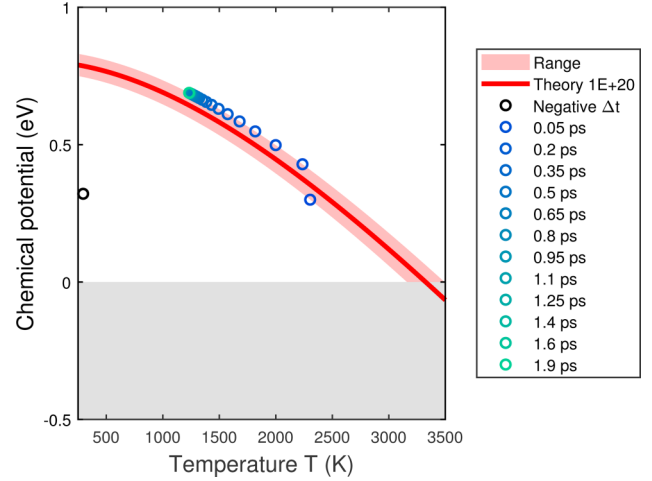

FIG. 7. Chemical potential extracted from fitting of the model to the experimental data, displayed as a function of the carrier temperature ($\circ$). For comparison, the red line shows the calculated chemical potential for a carrier density of $10^{20}\,\mathrm{cm}^{-3}$.

the analysis, we do not distinguish between specific scattering mechanisms. Instead, we approximated the overall energy relaxation by fitting the extracted values to a single exponential function of the form

$$\left\langle \frac{\mathrm{d}E(t)}{\mathrm{d}t} \right\rangle = \frac{Ae^{-\frac{t}{\tau}}}{\tau}, \tag{25}$$
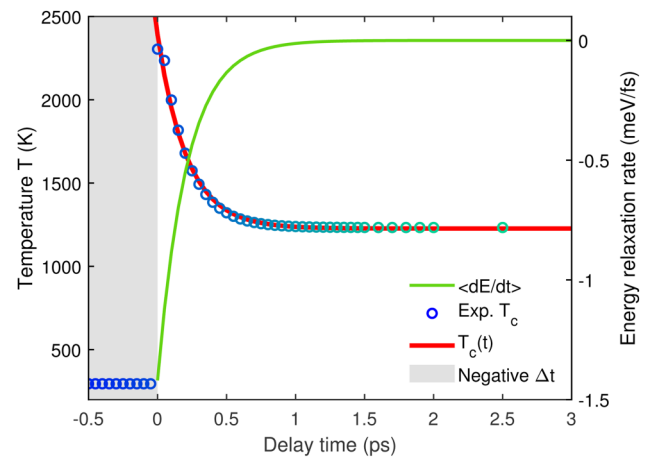

FIG. 8. The fitted carrier temperature is shown on the left axis by the circles ($\circ$) as a function of time delay. These experimentally obtained values are fitted with an exponential function, shown by the red line. On the right axis, the rate of energy relaxation is shown by the green line.

where A is a constant with energy units and $1/\tau$ is the overall relaxation rate. As stated before, the cooling of the carriers comes to a stall at around 1 ps. This is emphasized by the relaxation rate (shown by the green line in Fig. 8) calculated with Eq. (24). At delay times close to zero, we see the highest energy relaxation rate of the order of ~ 1.5 meV fs^{-1}. The phonon branches associated with intervalley scattering differ for each relaxation pathway (see Fig. 3). At room temperature, forbidden transverse acoustic (TA) and longitudinal optical (LO) phonons dominate the $\Gamma \rightarrow L$ scattering mechanism over the allowed longitudinal acoustic (LA) phonons.[36,55] For $\Gamma \rightarrow X$ and $X \rightarrow L$ scattering, the LO and transverse optical (TO) phonons are the dominant branches.[56] At the L-point, the phonon energies range from 8 to 36 meV,[57,58] whereas for the X-point, phonon energies range from 10 to 34 meV.[58] Quantitatively, we can infer that, at the highest relaxation rate, energy is being dissipated by emitting a phonon roughly every 5–24 femtoseconds. This result is within an order of magnitude with the literature intervalley scattering rates.[2,9,31,59]

Finally, the fitted energy parameters of the CPs are presented in Fig. 9. Under equilibrium conditions, the fitted critical point energies were found to be approximately 2.17 and 2.37 eV for the E_1 and $E_1 + \Delta_1$ transitions, respectively. These values are consistent with previously reported room temperature ellipsometry measurements of Ge.[46] Following photoexcitation, the CP energies present a redshift, most notably for the E_1 transition, which exhibits a shift of about 40 meV within the first few hundred femtoseconds. We emphasize that the most precise method for determining CP energies is through analysis of the 2nd derivative of the DF. Nevertheless, in our particular case, the energies for both fitting
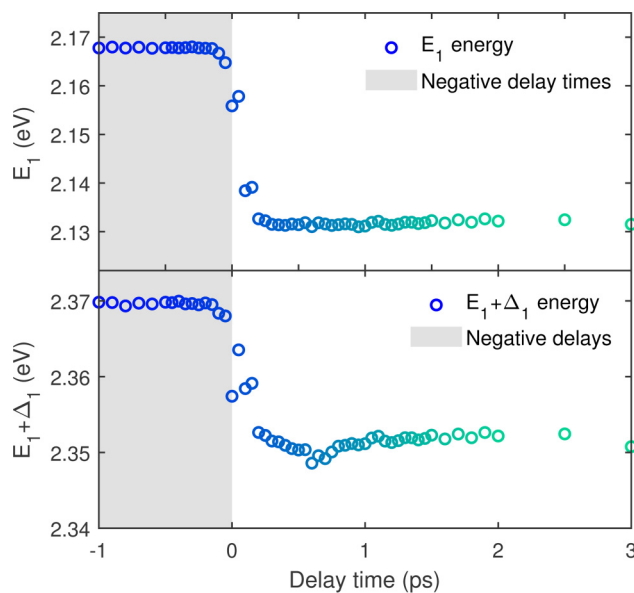

FIG. 9. Fitted energy parameters for the critical points E_1 and $E_1 + \Delta_1$. Negative delays (gray area) show the parameters for a steady-state measurement.

methods present a redshift for both CPs, even if the magnitude of the shift differs between the two approaches. As discussed in Sec. I B, this redshift is primarily attributed to bandgap renormalization effects due to many-body effects. While band filling can produce a competing blueshift in some systems by blocking lower energy transitions, this effect does not have an impact in the E_1 and $E_1 + \Delta_1$ CP energies in Ge. This has been demonstrated previously[39,47] and is further corroborated in our supplementary material (see Fig. S6 in Sec. S2). Consequently, we only observe a decrease in the transition energies. The redshifts for E_1 and $E_1 + \Delta_1$ are not the same. This might be due to strain induced by the laser excitation.

Overall, the combination of band-filling and excitonic effects provides a description of the ultrafast carrier dynamics in Ge. The temporal evolution of the chemical potential and the carrier temperature is consistent with intervalley scattering simulated in Sec. III B. Nonetheless, certain physical phenomena inherent to ultrafast processes, such as non-thermal carrier distributions and charge carrier screening of two-dimensional excitons, remain beyond the scope of the present work.

B. Limitations of the theory

Although the model captures the principal features of the transient response, several limitations should be mentioned. In particular, the incorporation of excitonic effects was restricted to their equilibrium states. However, at such high carrier densities, Coulomb interaction between electron-hole pairs is screened by the presence of additional carriers. Under strong excitation conditions, screening can significantly reduce exciton binding energies and alter the oscillator strength of the absorption states near the CPs. For three-dimensional excitons, Tanguy provided an expression for the optical response by solving the Schrödinger equation for the Hulthén potential.[60,61] Furthermore, this expression has already been applied to Ge by describing the direct bandgap E_0. These published efforts indicate that the reduction in the amplitude of ε_2 should be induced by excitonic screening in addition to band-filling effects. However, an expression for the optical response of screened two-dimensional excitons does not exist in the literature.[62–65] For this reduced dimensionality problem, recent efforts have found the binding energy for screened excitons in two-dimensional materials (these are solutions to the Rytova–Keldysh potential).[66,67] Unfortunately, an expression of the DF for this potential is yet to be given.

The results of Fig. 6 show that at around 1 ps, the amplitude of ε_2 reaches its maximum change and remains nearly constant thereafter. This is further corroborated in Fig. 7, where the chemical potential stays approximately constant around this time, suggesting that the carrier cooling has stopped. Excitonic screening affects the amplitude of ε_2 in a similar fashion to an increase of the chemical potential (see Sec. S6 in the supplementary material). Thus, the initial reduction in the amplitude of the DF cannot be solely caused by the lifting of the quasi-Fermi level, but a combination of band-filling and excitonic screening. A comprehensive theoretical framework that explicitly incorporates screened excitonic effects is, therefore, essential for a more complete description of the transient dielectric response.

Additionally, the model assumes a single effective carrier temperature and a Fermi–Dirac distribution at all time delays, thereby ignoring possible non-thermal carrier distributions immediately after excitation. While it is reasonable to assume that dephasing occurs almost instantaneously (of the order of tens of femtoseconds),[59,68] thermalization typically unfolds over longer timescales.[25,69] These simplifications, although necessary for our model, limit the ability to describe the optical response in the earliest relaxation stages. Despite these limitations, our model provides a good qualitative description of the transient optical response. However, a complete treatment of screened excitonic effects and non-thermal carrier distributions remains an open subject for further investigation.

VI. SUMMARY

In this work, we utilized a broadband femtosecond spectroscopic ellipsometry setup to investigate the ultrafast carrier dynamics in Ge under strong optical excitation. By analyzing the TDF, we were able to probe the time-dependent optical response of the material under non-equilibrium conditions. To model the optical spectra, we incorporated band-filling effects into a two-dimensional excitonic line shape. The model successfully reproduced the main features of the TDF, such as the decrease in the amplitude of ε_2 due to the filling of the bands. From the fits, we extracted the temporal evolution of the carrier temperature and the chemical potential, which were found to be consistent with our intervalley scattering and thermalization dynamics calculations. Additionally, we observed redshifts in the CP energies, which we attribute primarily to bandgap renormalization effects. Furthermore, we determined an energy relaxation rate of approximately $1.5\,\mathrm{meV\,fs^{-1}}$, which provides a measure of the cooling of the carriers.

While the model effectively reproduces the main spectral features, it relies on several assumptions. In particular, it assumes instantaneous dephasing and thermalized carrier distributions at each delay time, thus excluding possible non-thermal carrier populations immediately after excitation. Additionally, a treatment of the dielectric screening for two-dimensional excitons is entirely omitted. These simplifications limit the applicability of our theory to the earliest delay times and make a detailed description of the coherent regime impossible. Nonetheless, the framework developed here provides a model that describes the ultrafast carrier dynamics and many-body effects in semiconductors qualitatively. This work can be extended to other materials and excitation regimes to further explore the physics of ultrafast optical phenomena.

SUPPLEMENTARY MATERIAL

See the supplementary material for details on the data acquisition and reduction process. A detailed derivation of our band-filling model is also included. Furthermore, we include a calculation of the chemical potential for an intrinsic semiconductor at room temperature. We also discuss how the 2nd derivatives are obtained numerically using the EG digital filter. Finally, we present the real part of the DF.

AUTHOR DECLARATIONS

Conflict of Interest

The authors have no conflicts to disclose.

Author Contributions

C. A. Armenta: Conceptualization (equal); Data curation (equal); Formal analysis (equal); Investigation (equal); Methodology (equal); Software (equal); Validation (equal); Visualization (equal); Writing – original draft (equal); Writing – review & editing (equal). **M. Zahradník:** Data curation (equal); Formal analysis (equal); Methodology (equal); Software (equal); Writing – review & editing (equal). **M. Rebarz:** Data curation (supporting); Formal analysis (supporting); Methodology (equal); Writing – review & editing (supporting). **C. Emminger:** Data curation (equal); Software (equal). **S. Espinoza:** Methodology (supporting); Resources (lead); Supervision (equal). **S. Vazquez-Miranda:** Data curation (supporting); Methodology (supporting); Software (supporting). **J. Andreasson:** Resources (supporting); Supervision (supporting). **S. Zollner:** Conceptualization (equal); Formal analysis (equal); Funding acquisition (equal); Investigation (equal); Project administration (equal); Resources (equal); Supervision (equal); Validation (equal); Visualization (equal); Writing – review & editing (equal).

DATA AVAILABILITY

The data that support the findings of this study are available from the corresponding author upon reasonable request.

REFERENCES

[1]H. Kalt and C. F. Klingshirn, *Semiconductor Optics 2: Dynamics, High-Excitation Effects, and Basics of Applications* (Springer, Cham, 2024).

[2]J. Shah, *Ultrafast Spectroscopy of Semiconductors and Semiconductor Nanostructures* (Springer, New York, 1999).

[3]S. Richter, M. Rebarz, O. Herrfurth, S. Espinoza, R. Schmidt-Grund, and J. Andreasson, Rev. Sci. Instrum. **92**, 033104 (2021).

[4]S. Richter, O. Herrfurth, S. Espinoza, M. Rebarz, M. Kloz, J. A. Leveillee, A. Schleife, S. Zollner, M. Grundmann, J. Andreasson, and R. Schmidt-Grund, New J. Phys. **22**, 083066 (2020).

[5]S. Espinoza, S. Richter, M. Rebarz, O. Herrfurth, R. Schmidt-Grund, J. Andreasson, and S. Zollner, Appl. Phys. Lett. **115**, 052105 (2019).

[6]S. Zollner, K. D. Myers, J. M. Dolan, D. W. Bailey, and C. J. Stanton, Thin Solid Films **313–314**, 568 (1998).

26 November 2025 16:22:58

[7]C. Emminger, S. Espinoza, S. Richter, M. Rebarz, O. Herrfurth, M. Zahradník, R. Schmidt-Grund, J. Andreasson, and S. Zollner, Phys. Status Solidi RRL **16**, 220058 (2022).

[8]B. R. Nag, in *Semiconductors Probed by Ultrafast Laser Spectroscopy Volume I*, edited by R. R. Alfano (Academic, Orlando, FL, 1984), p. 3.

[9]J. Shah and R. F. Leheny, in *Semiconductors Probed by Ultrafast Laser Spectroscopy Volume I*, edited by R. R. Alfano (Academic, Orlando, FL, 1984), p. 45.

[10]P. Vashishta and R. K. Kalia, Phys. Rev. B **25**, 6492 (1982).

[11]T. S. Moss, Proc. Phys. Soc. B **67**, 775 (1954).

[12]E. Burstein, Phys. Rev. **93**, 632 (1954).

[13]H. Schweizer, A. Forchel, A. Hangleiter, S. Schmitt-Rink, J. P. Löwenau, and H. Haug, Phys. Rev. Lett. **51**, 698 (1983).

[14]B. A. Magill, R. R. H. H. Mudiyanselage, T. Paleologu, C. E. McKinney, Y. Pleimling, N. W. G. Smith, M. Hudait, C. J. Stanton, and G. A. Khodaparast, Phys. Rev. B **112**, 075308 (2025).

[15]G. A. Thomas, T. M. Rice, and J. C. Hensel, Phys. Rev. Lett. **33**, 219 (1974).

[16]E. Baron, R. Goldhahn, S. Espinoza, M. Zahradník, M. Rebarz, J. Andreasson, M. Deppe, D. J. As, and M. Feneberg, J. Appl. Phys. **134**, 075702 (2023).

[17]E. Baron, R. Goldhahn, S. Espinoza, M. Zahradník, M. Rebarz, J. Andreasson, M. Deppe, D. J. As, and M. Feneberg, J. Appl. Phys. **134**, 075703 (2023).

[18]A. Othonos, H. M. van Driel, J. F. Young, and P. J. Kelly, Phys. Rev. B **43**, 6682 (1991).

[19]A. Othonos, J. Appl. Phys. **83**, 1789 (1998).

[20]See https://www.coherent.com/ for product information about the lasers used for our experiments.

[21]H. Fujiwara, *Spectroscopic Ellipsometry: Principles and Applications* (Wiley, Chichester, 2007).

[22]T. N. Nunley, N. S. Fernando, N. Samarasingha, J. M. Moya, C. M. Nelson, A. A. Medina, and S. Zollner, J. Vac. Sci. Technol. B **34**, 061205 (2016).

[23]C. Emminger, F. Abadizaman, N. S. Samarasingha, T. E. Tiwald, and S. Zollner, J. Vac. Sci. Technol. B **38**, 012202 (2020).

[24]See https://www.jawoollam.com/ for information about the J. A. Woollam Company.

[25]X. Q. Zhou, H. M. van Driel, and G. Mak, Phys. Rev. B **50**, 5226 (1994).

[26]A. I. Lobad, Y. Kostoulas, G. W. Wicks, and P. M. Fauchet, in *Hot Carriers in Semiconductors*, edited by K. Hess, J. P. Leburton, and U. Ravaioli (Plenum, New York, 1996), p. 97.

[27]A. L. Smirl, in *Physics of Nonlinear Transport in Semiconductors*, edited by D. K. Ferry, J. R. Barker, and C. Jacoboni (Plenum, New York, 1980), p. 367.

[28]P. Tognini, A. Stella, S. De Silvestri, M. Nisoli, S. Stagira, P. Cheyssac, and R. Kofman, Appl. Phys. Lett. **75**, 208 (1999).

[29]M. Zürch, H.-T. Chang, L. J. Borja, P. M. Kraus, S. K. Cushing, A. Gandman, C. J. Kaplan, M. H. Oh, J. S. Prell, D. Prendergast, C. D. Pemmaraju, D. M. Neumark, and S. R. Leone, Nat. Commun. **8**, 15734 (2017).

[30]A. Elci, M. O. Scully, A. L. Smirl, and J. C. Matter, Phys. Rev. B **16**, 191 (1977).

[31]S. Zollner, S. Gopalan, and M. Cardona, Solid State Commun. **76**, 877 (1990).

[32]W. B. Wang, M. A. Cavicchia, and R. R. Alfano, in *Hot Carriers in Semiconductors*, edited by K. Hess, J. P. Leburton, and U. Ravaioli (Plenum, New York, 1996), p. 101.

[33]A. L. Smirl, in *Semiconductors Probed by Ultrafast Laser Spectroscopy Volume I*, edited by R. R. Alfano (Academic, Orlando, 1984), p. 198.

[34]M. Grundmann, *The Physics of Semiconductors: An Introduction Including Nanophysics and Applications* (Springer, Cham, 2021).

[35]See https://www.mathworks.com/ for product information about the software used for data analysis and graphical display of results.

[36]J. Menéndez, C. D. Poweleit, and S. E. Tilton, Phys. Rev. B **101**, 195204 (2020).

[37]J. Menéndez, D. J. Lockwood, J. C. Zwinkels, and M. Noël, Phys. Rev. B **98**, 165207 (2018).

[38]D. E. Aspnes, Phys. Rev. B **12**, 2297 (1975).

[39]C. Xu, J. Kouvetakis, and J. Menéndez, J. Appl. Phys. **125**, 085704 (2019).

[40]M. Cardona and F. H. Pollak, Phys. Rev. **142**, 530 (1966).

[41]M. B. Clavel, F. Murphy-Armando, Y. Xie, K. T. Henry, M. Kuhn, R. J. Bodnar, G. A. Khodaparast, D. Smirnov, J. J. Heremans, and M. K. Hudait, Phys. Rev. Appl. **18**, 064083 (2022).

[42]G. Dresselhaus, A. Kip, and C. Kittel, Phys. Rev. **98**, 368 (1955).

[43]H. Kalt and M. Rinker, Phys. Rev. B **45**, 1139 (1992).

[44]P. Y. Yu and M. Cardona, *Fundamentals of Semiconductors: Physics and Materials Properties* (Springer, Berlin, 1996).

[45]C. Tanguy, Solid State Commun. **98**, 65 (1996).

[46]C. A. Armenta and S. Zollner, J. Appl. Phys. **137**, 245701 (2025).

[47]C. Xu, N. S. Fernando, S. Zollner, J. Kouvetakis, and J. Menéndez, Phys. Rev. Lett. **118**, 267402 (2017).

[48]S. Zollner, C. A. Armenta, S. Yadav, and J. Menéndez, J. Vac. Sci. Technol. A **43**, 012801 (2025).

[49]J. W. Garland, C. Kim, H. Abad, and P. M. Raccah, Phys. Rev. B **41**, 7602 (1990).

[50]J. W. Garland, C. C. Kim, H. Abad, and P. M. Raccah, Thin Solid Films **233**, 148 (1993).

[51]D. E. Aspnes and H. Arwin, J. Opt. Soc. Am. **73**, 1759 (1983).

[52]V. L. Le, T. J. Kim, Y. D. Kim, and D. E. Aspnes, J. Vac. Sci. Technol. B **37**, 052903 (2019).

[53]D. K. Hoffman, D. J. Kouri, and E. Pollak, Comput. Phys. Commun. **147**, 759 (2002).

[54]W. Pötz and P. Kocevar, in *Hot Carriers in Semiconductor Nanostructures: Physics and Applications*, edited by J. Shah (Academic, San Diego, CA, 1992), p. 87.

[55]G. A. Thomas, E. I. Blount, and M. Capizzi, Phys. Rev. B **19**, 702 (1979).

[56]V. G. Tyuterev, S. V. Obukhov, N. Vast, and J. Sjakste, Phys. Rev. B **84**, 035201 (2011).

[57]R. R. Lieten, K. Bustillo, T. Smets, E. Simoen, J. W. Ager III, E. E. Haller, and J.-P. Locquet, Phys. Rev. B **86**, 035204 (2012).

[58]G. Nilsson and G. Nelin, Phys. Rev. B **6**, 3777 (1972).

[59]D. W. Bailey and C. J. Stanton, J. Appl. Phys. **77**, 2107 (1995).

[60]C. Tanguy, Phys. Rev. B **75**, 4090 (1995).

[61]C. Tanguy, Phys. Rev. B **60**, 10660 (1999).

[62]F. Stern and W. E. Howard, Phys. Rev. **163**, 816 (1967).

[63]D. G. W. Parfitt and M. E. Portnoi, Physica E **17**, 212 (2003).

[64]D. G. W. Parfitt and M. E. Portnoi, in *Mathematical Physics, Proceedings of the XI Regional Conference, Tehran, Iran, 3–6 May 2004* (World Scientific, Singapore, 2005), p. 52.

[65]A. J. Makowski, Phys. Rev. A **84**, 022108 (2011).

[66]M. R. Molas, A. O. Slobodeniuk, K. Nogajewski, M. Bartos, Ł. Bala, A. Babiński, K. Watanabe, T. Taniguchi, C. Faugeras, and M. Potemski, Phys. Rev. Lett. **123**, 136801 (2019).

[67]H. T. Nguyen-Truong, Phys. Rev. B **105**, L201407 (2022).

[68]P. C. Becker, H. L. Fragnito, C. H. Brito Cruz, R. L. Fork, J. E. Cunningham, J. E. Henry, and C. V. Shank, Phys. Rev. Lett. **61**, 1647 (1988).

[69]C. Lange, N. S. Köster, S. Chatterjee, H. Sigg, D. Chrastina, G. Isella, H. von Känel, B. Kunert, and W. Stolz, Phys. Rev. B **81**, 045320 (2010).

26 November 2025 16:22:58